JOURNAL OF MATERIALS SCIENCE 30 (1995) 3680–3689

The structure of a rapidly solidified Al–Fe–Ti–C alloy

X. C. TONG, N. F. SHEN
Research Centre for Materials, Zhengzhou Institute of Technology, Zhengzhou 450002, People's Republic of China
B. C. LIU
Department of Mechanical Engineering, Tsinghua University, Beijing 100084, People's Republic of China

The microstructures of melt-spun Al–2.03 Fe–0.46 Ti–0.35 C (at %) superheated to 1523 K (ribbon I), and 1673 K (ribbon II), respectively, before quenching, have been characterized using analytical electron microscopy and X-ray diffraction. A duplex microstructure has been observed for ribbon I, consisting of a microcellular region, across a sharp transition, followed by a coarser cellular or dendritic structure. The intercellular phases consisted mostly of Al_6Fe (few of Al_3Fe) and the dispersed TiC particles distributed in the α–Al matrix with an exact orientation relationship. However, the microstructure of ribbon II comprised uniform, fine-scale dispersions of Al_6Fe phase in α–Al grains, and larger size, elongated amorphous phase particles located along the grain boundaries, and approximately 0.46 at % Ti and 0.35 at % C dissolved in the α–Al matrix. During the annealing of ribbon II, the amorphous phase transformed to α_T-AlFeSi phase, the Al_6Fe dispersoids grew upwards and Al_3Fe, TiC particles precipitated in the α-Al matrix. TiC phase formed both in ribbon I and in annealed ribbon II all had an atomic composition of $TiC_{0.79}$ (the nominal atomic percent ratio for the alloy X_C/X_{Ti} was 0.74) and a lattice parameter of 0.424 nm. Moreover, there is a cube–cube orientation relationship between TiC and α-Al matrix with a disregistry $\delta = 0.049$. In addition, the solidification characteristics of rapid solidification processing (RSP) Al–Fe–Ti–C alloy and mechanism of TiC formation have been discussed.

1. Introduction

Improved strength at elevated temperatures has been a continuing goal in aluminium alloy development. Presently, development of high-temperature ($T > 0.5\,T_m$) aluminium alloys for structural applications has been mainly focused on dispersion strengthening as a means to reduce dislocation-assisted creep rates. Desirable microstructures consist of a high volume fraction distribution of fine, hard intermetallic phase particles which resist further transformation or coarsening at the operating temperature. Low coarsening rates are generally favoured by low diffusivities of the alloying elements and low interfacial energy of intermetallic phases in an aluminium matrix. In this context, a majority of the alloys under consideration involves the Al–Fe system with ternary or quaternary additions of Cr, Mo(+ Si), Zr, V(+ Si), Ce and W etc. [1–3]. Meanwhile, microstructural refinement arising from rapid solidification processing (RSP) offers a potential avenue to alleviate the macrosegregation and enhance the dispersion hardening effects by substantially reducing the size scale of the intermetallic phases. Al–Fe is an attractive system due to the extent to which its microstructure can be altered by RSP. In particular, the production of fine dispersoids that exhibit unusually low coarsening rates forms the basis for most of the high-temperature aluminium alloys developed to date. However, supposing that a dispersed TiC phase could form *in situ* in the Al–Fe system by adding Ti and C elements, a new alloy of Al–Fe–Ti–C would cause more interest in engineering applications because the TiC phase itself has high values of strength and hardness, a very high melting point, and superior stability at high temperatures. The purpose of the present study is to investigate the microstructural characteristics of the RSP Al–Fe–Ti–C alloy and possible phase transformations during its annealing. Moreover, the formation mechanism of TiC dispersoids and their probable function as heterogeneous nucleation sites for α-Al will be explored.

2. Experimental procedure

The Al–Fe–Ti–C alloy ingots were prepared from 99.9% Al, 99.7% Ti, medium carbon steel and graphite particles of ~1 mm average particle size, which were induction-melted under argon in a graphite crucible. The ingot alloy had a chemical composition (at %) 2.03 Fe, 0.46 Ti, 0.35 C, 0.64 Si and the balance was aluminium. Rapidly solidified samples were

0022–2461

prepared by chill block melt-spinning. Alloy charges of approximately 20 g were remelted in quartz crucibles under a dynamic Ar atmosphere, using a calibrated pyrometer to monitor alloy temperatures. When the temperature rose to a given value, the molten alloy was ejected with an Ar overpressure of 60 KPa through an orifice onto the periphery surface of a copper drum rotating with a surface linear velocity of $30\,m\,s^{-1}$. To examine the influence of the level of superheating of the liquid alloy on the final structures, the melting temperatures (a) 1523 K and (b) 1673 K for 5 min were selected. The ribbons obtained were approximately 5 mm in width and (a) 80 ~ 90 µm, (b) 40 ~ 50 µm in thickness, and were designated ribbon I and ribbon II, respectively. Sections of ribbon II were subsequently heat-treated in a graphite powder bath at 573 K for 6 h, 633 K for 5 h, 673 K for 48 and 96 h and 773 K for 5 h to examine the thermal stability and phase transformations during annealing.

Thin foils for transmission electron microscopy (TEM) were prepared firstly by jet electropolishing using an electrolyte of glycerin and perchloric acid in methanol, and then jet ion milling. TEM examinations were performed in a Jeol-2000FX transmission electron microscope equipped with a Link AN-10000 energy dispersive X-ray spectrometer (EDS). Electron energy loss spectrum (EELS) analyses were carried out in a Philips CM12 transmission electron microscope interlaced to a GATAN666 facility, using P absorption edge. X-ray diffractions of the ribbons were carried out using a Philips PW 1700 instrument with CuK_α radiation.

3. Results

3.1. Rapidly solidified ribbons

3.1.1. *Observation on ribbon I*

For ribbon I with thickness of between 80 and 90 µm, a duplex microstructure has been observed for the alloy superheated to 1523 K before quenching. The typical microstructure of a two-side thinned sample is shown in Fig. 1(a). The as-cast microstructure was strongly dependent on its location in the ribbon and can be distinguished by two regions – microcellular (A) and coarse cellular (C), with a sharp transition region (B) from the microcellular to the coarse cellular structure. The microcellular region (zone A) contained a very fine segregation pattern with the cell spacing ranging from 0.04 to 0.06 µm. A gradual coarsening of the pattern, or more frequently, a sharp transition (B) from zone A to zone C, in which there was a much coarser pattern, has been observed. At the transition, cell spacing increased about 10 times (0.4 ~0.6 µm). In zone C, some regions consisted of cellular structure (0.4 to 0.8 µm in size) whilst others comprised dendritic structure, which resembled a partially coarsened segregation. The overriding features of the microstructure lay in their heterogeneous nature, being in agreement with previous studies on the splat-quenched and gas-atomized alloys of the Al–Fe system [4–7].

At the same time, a variation of phases constituting the second phase net-work was observed associated with an increasing phase interspacing. Fig. 1(b) and (c) are the characteristic diffraction patterns from intercellular phases of zones A and C, respe ctively. The indexing of these diffraction patterns leads us to the conclusion that most of intercellular phases were

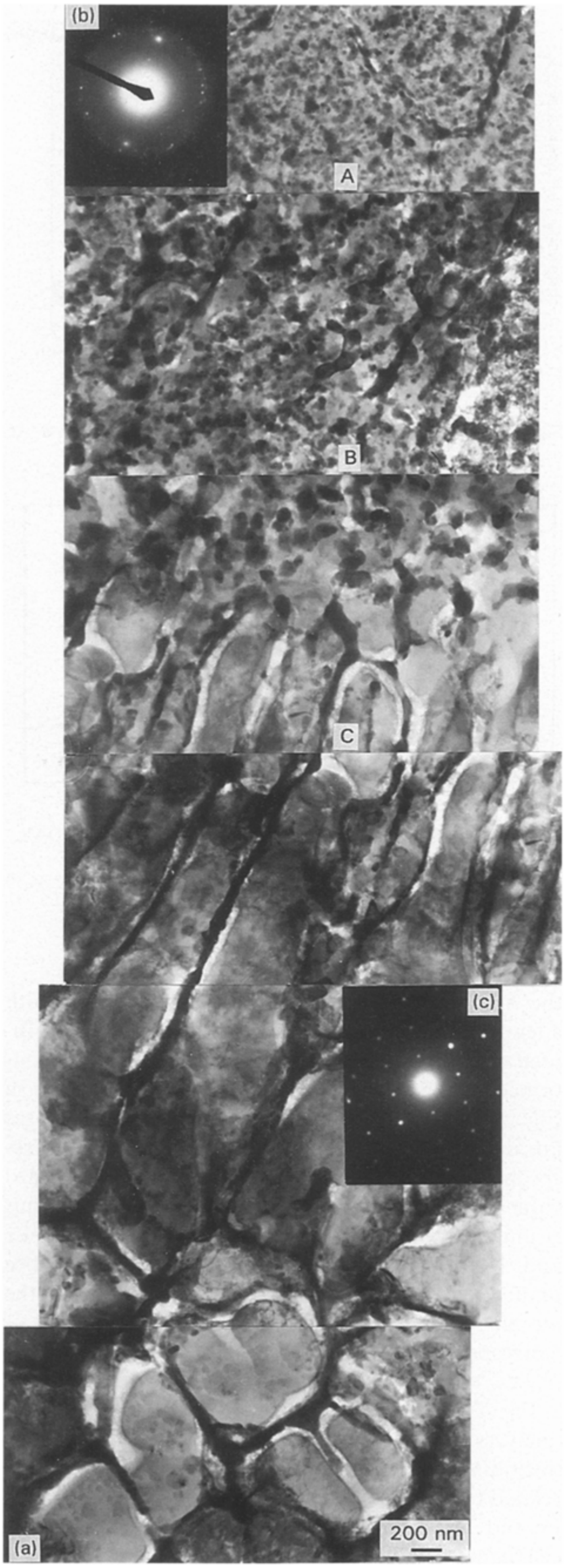

Figure 1 (a) TEM micrograph showing microstructure variation in ribbon I; (b) SAED pattern from zone A; (c) SAED pattern from the intercellular phase of zone. C.

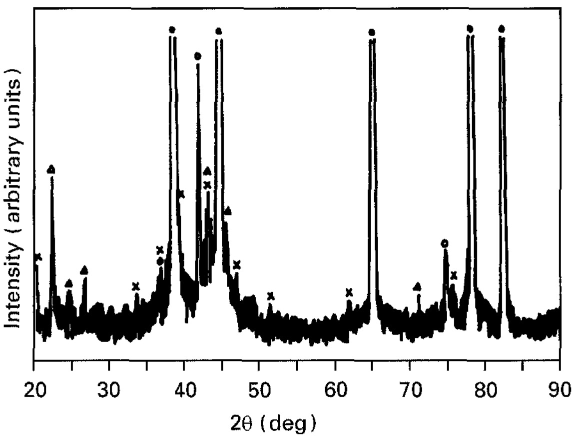

Figure 2 X-ray diffraction pattern of the as-cast ribbon I. ● Al; × Al_6 Fe; △ Al_3Fe; ○ TiC.

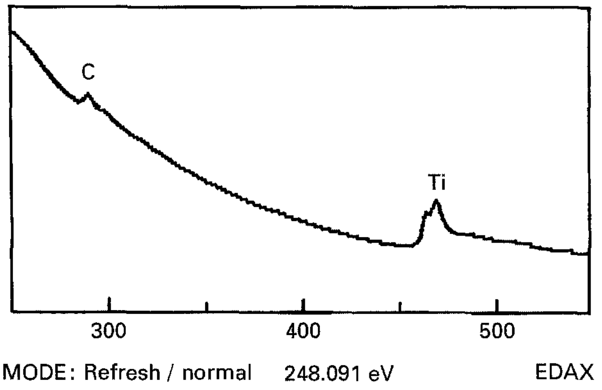

Figure 3 EELS analysis data of TiC phase in ribbon I. C, K 44.19 at %, $\sigma = 2.828 \times 10^{-21}$; Ti, L 55.81 at %, $\sigma = 1.336 \times 10^{-21}$.

the Al_6Fe metastable phase, probably together with a few of the Al_3Fe phase, while the TiC phase distributed on the α-Al matrix. These results were also confirmed by the X-ray diffraction analyses, as shown in Fig. 2. The lattice parameters of α-Al and TiC phases are determined to be 0.4031 nm and 0.4240 nm, respectively. All of them are less than their standard values (0.40496 nm and 0.4318 nm respectively). This is understandable because the supersaturation of Fe and Ti in α-Al matrix tends to decrease its lattice parameter [8], however, EELS analysis shows the atomic composition of the TiC phase is $TiC_{0.79}$ (corresponding to the atomic percentage ratio $X_c/X_{Ti} = 0.74$) not TiC_1, as shown in Fig. 3.

Fig. 4 summarizes the results obtained from EDS analyses for the average compositions of the matrix (including the second phase particles over a region related to the probe size and the space resolution) and Fe and Ti contents inside α-Al cells as a function of cell diameter (Si is present in intermetallic compounds, e.g. Al_6Fe, Al_3Fe). The mean Fe content of as-solidified structures were a function of phase interspacing (curve a). Note that the solute content retained about the same concentration of the parent alloy at the smaller interspacing. A increasing trend of the Fe content was detected inside cells below 250 nm in diameter (curve b). In contrast to this, low Fe contents were detected in cells with larger diameters ($d_c > 250$ nm). EDS showed flat solute profiles along cell interiors with strong solute segregation at cell boundaries. However, the mean Ti contents and the Ti content inside cells all showed relatively flat variation with the cell diameter, while the mean Ti content is slightly lower than that of the cell interior. These imply that the sole Ti-enriched phase $TiC_{0.79}$ distributes uniformly on the α-Al matrix or slightly more in the intracellular regions than in the intercellular regions.

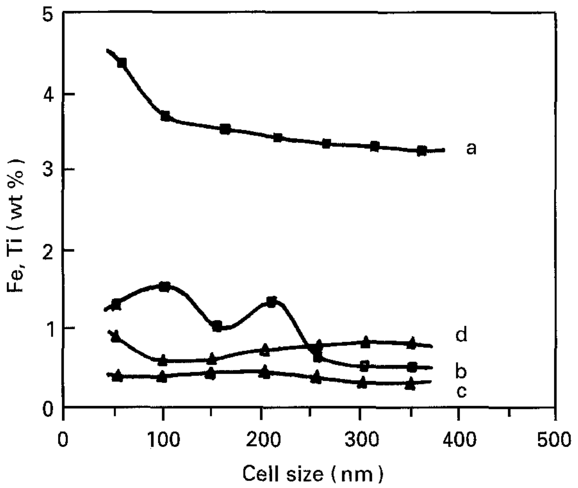

Figure 4 EDS microanalysis data of the variation of average composition for the region of "α-Al + dispersoids" (curve a for Fe and c for Ti) and the variation of Fe (curve b), Ti (curve d) – contents inside cells as a function of cell diameter.

3.1.2. Observations on ribbon II

For ribbon II, a fine microstructure consisted of α-Al grains from 0.15 to 0.30 μm in size has been observed, as shown in Fig. 5. The intermetallic particles with average size of 10 to 50 nm distributed uniformly on the α-Al matrix and orientated randomly with respect to the α-Al matrix. Larger size and elongated particles are usually located along subgrain or grain boundaries. Microdiffraction analyses showed that these particles have an amorphous structure (Fig. 5(d)), while EDS analyses indicated that this amorphous phase had a composition of 66.9 wt % Al, 27.9 wt % Fe and 5.2 wt % Si. Note that its Fe content is close to that of Al_6Fe (25.6 wt % Fe). In fact, this amorphous phase is not "normal" metallic glass (dense random packing model) but probably similar to that observed in binary Al–Fe and called "S" phase by Shechtman [9]. Much smaller size and globular particles are embedded in the α-Al matrix grains. The indexing of the characteristic diffraction rings (Fig. 5(c)) from the globular particles had revealed its Al_6Fe metastable phase structure. In the sample, no Ti and/or C-enriched phases were found and EDS and EELS analyses confirmed that the Ti and C contents (Fig. 6) dissolved in the α-Al were close to the nominal alloy composition of 0.46 and 0.35 at %, respectively. However, besides α-Al and Al_6Fe diffraction peaks, no obvious amorphous phase characteristic peaks could be seen in the X-ray diffraction pattern (Fig. 7), showing that the volume fraction of the amorphous phase is considerably small compared with α-Al and Al_6Fe phases.

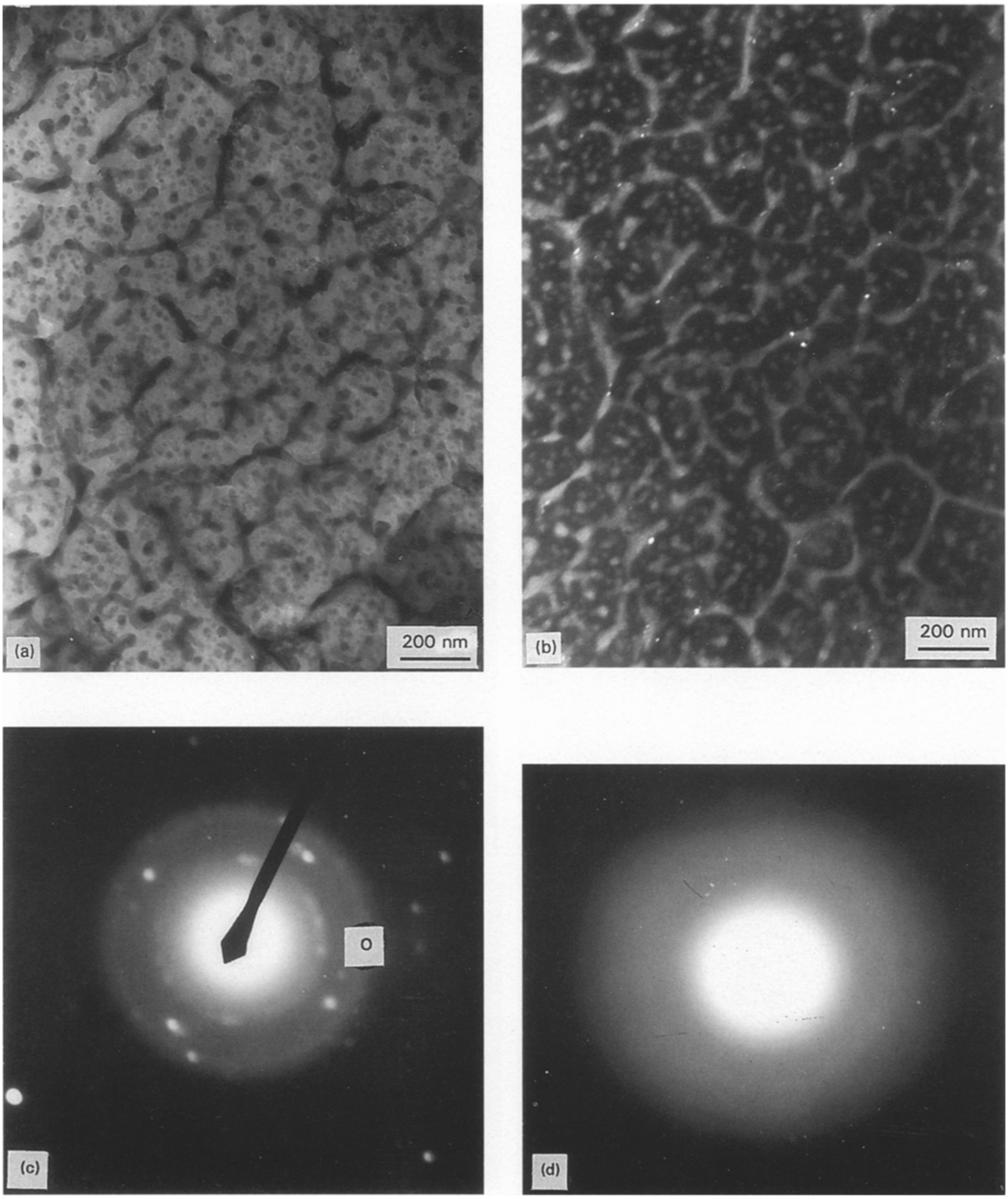

Figure 5 Bright-field (a) and dark-field (b) TEM images of ribbon II and the corresponding selected area diffraction pattern (c) and microdiffraction pattern from elongated particles along grain or subgrain boundaries (d). (b) shows the position of the objective area aperture and identified features are individual reflection from α-Al matrix, diffuse rings from amorphous elongated phase, and spotty rings from particles of the globular Al_6Fe phase.

3.2. Phase transformation during annealing of ribbon II

The decomposition of the metastable rapidly solidified microstructure of ribbon II was studied sequentially by isochronal annealing. The microstructure of the ribbon annealed at 573 K for 6 h remained the features of the as-solidified microstructure except that the elongated particles located along subgrain boundaries became much coarser (Fig. 8(a)). For the ribbon annealed at 633 K for 5 h, the α-Al grains have grown up to 0.6 ± 0.1 μm while the globular particles appeared to be slightly coarser and the elongated particles have been replaced by larger and polygonal particles (~ 0.1 μm) with a composition near that of the amorphous phase in as-solidified structures, and a needle-like phase (0.08 × 0.3 μm) with a composition of 62.7 wt % Al and 37.3 wt % Fe appeared near the grain boundaries (Fig. 8(b)). After annealing at 673 K for 48 h, all the intermetallic phase particles have been replaced by much coarser polygonal particles,

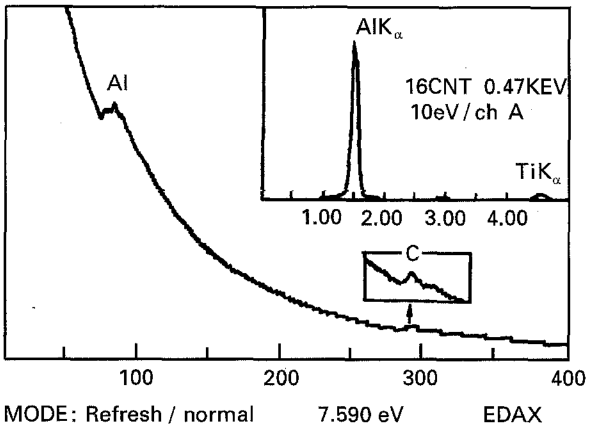

Figure 6 EELS analysis data of Ti, C- contents inside cells of α-Al in ribbon II.

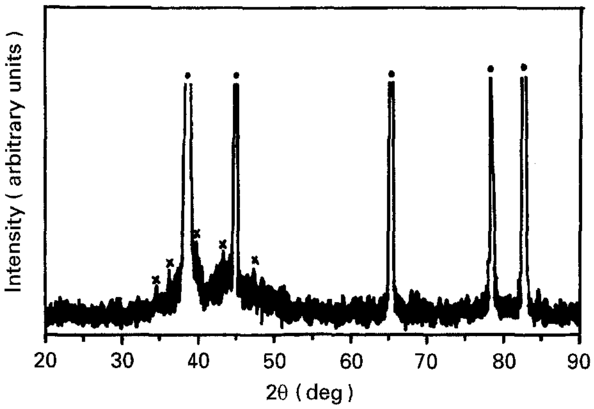

Figure 7 X-ray diffraction of the as-cast ribbon II. ● Al; × Al_6Fe.

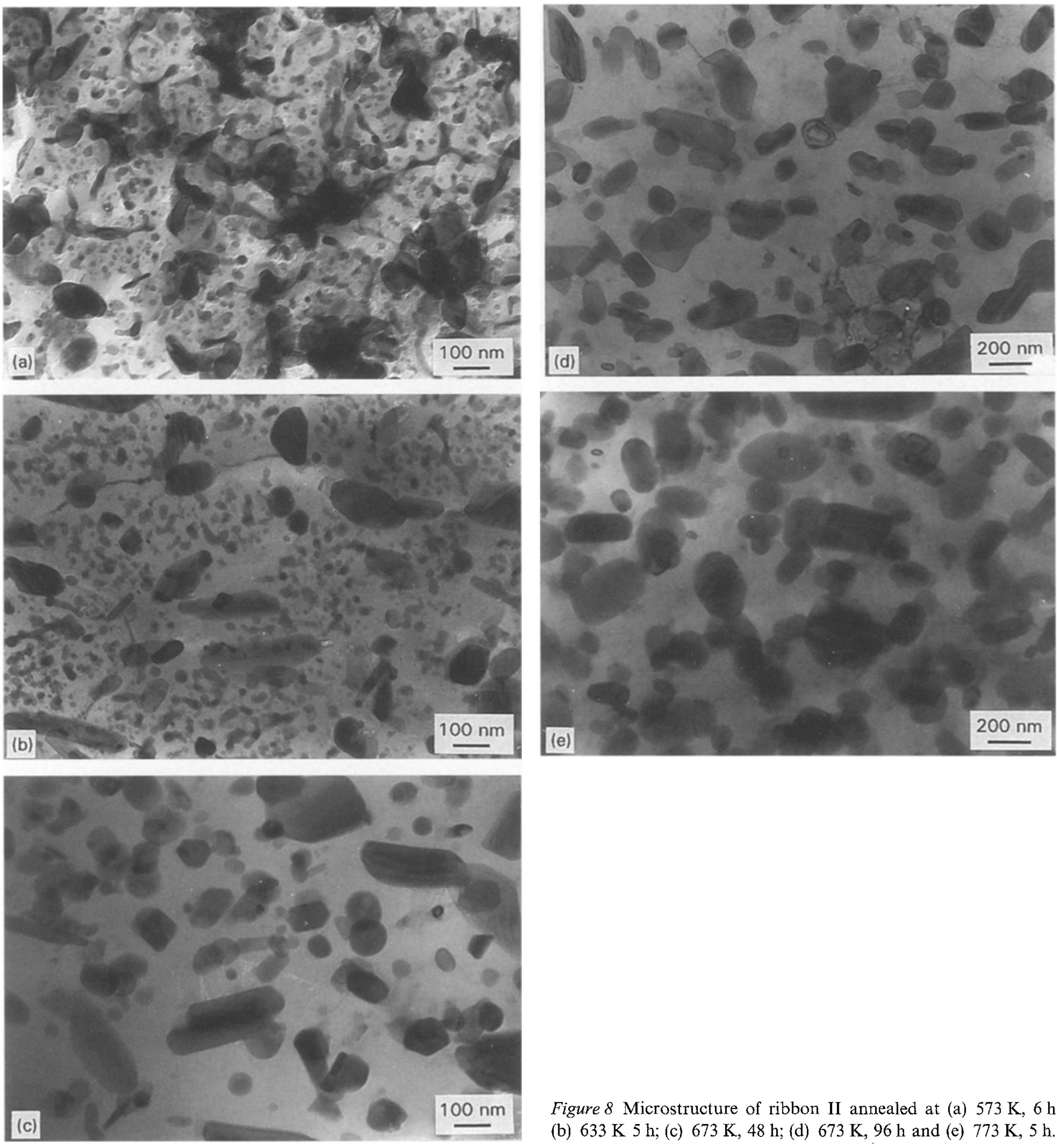

Figure 8 Microstructure of ribbon II annealed at (a) 573 K, 6 h; (b) 633 K 5 h; (c) 673 K, 48 h; (d) 673 K, 96 h and (e) 773 K, 5 h.

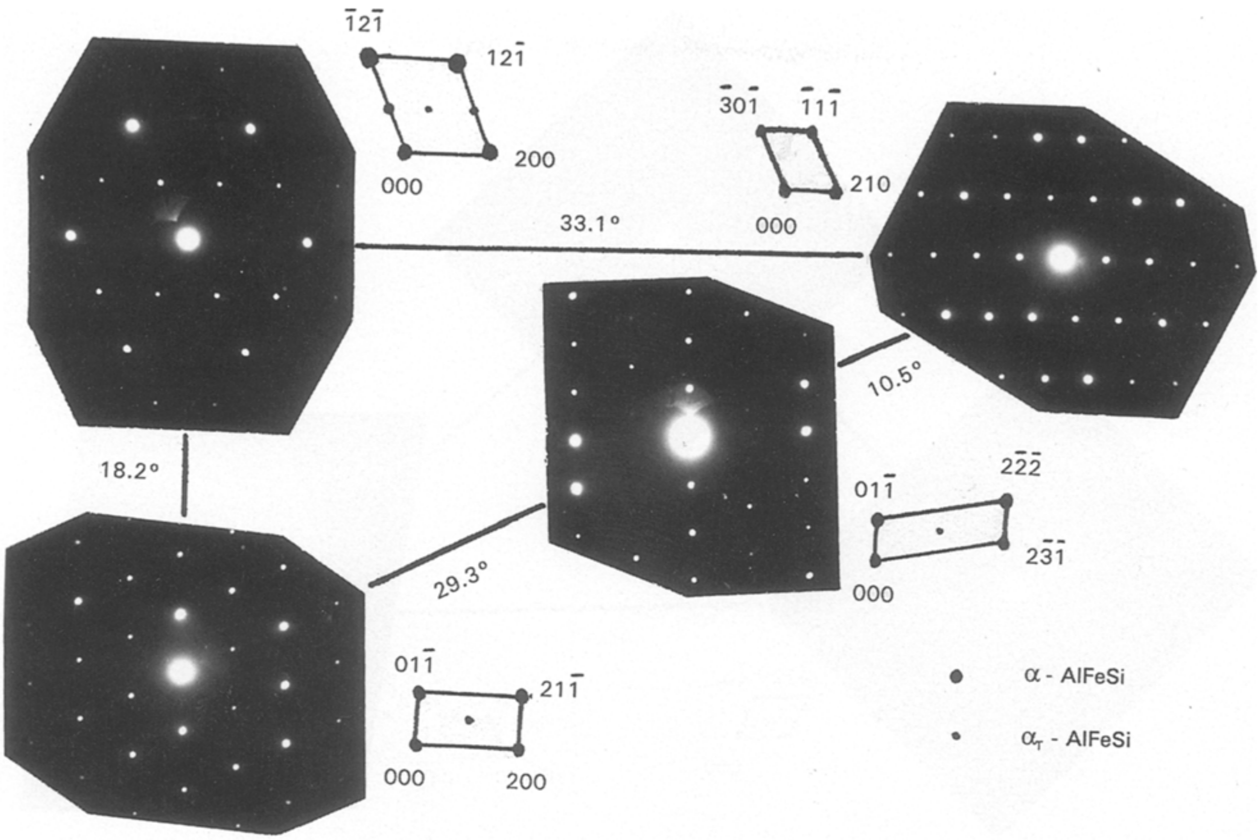

Figure 9 A series of diffraction patterns of α_T-AlFeSi from Fig. 8 (e).

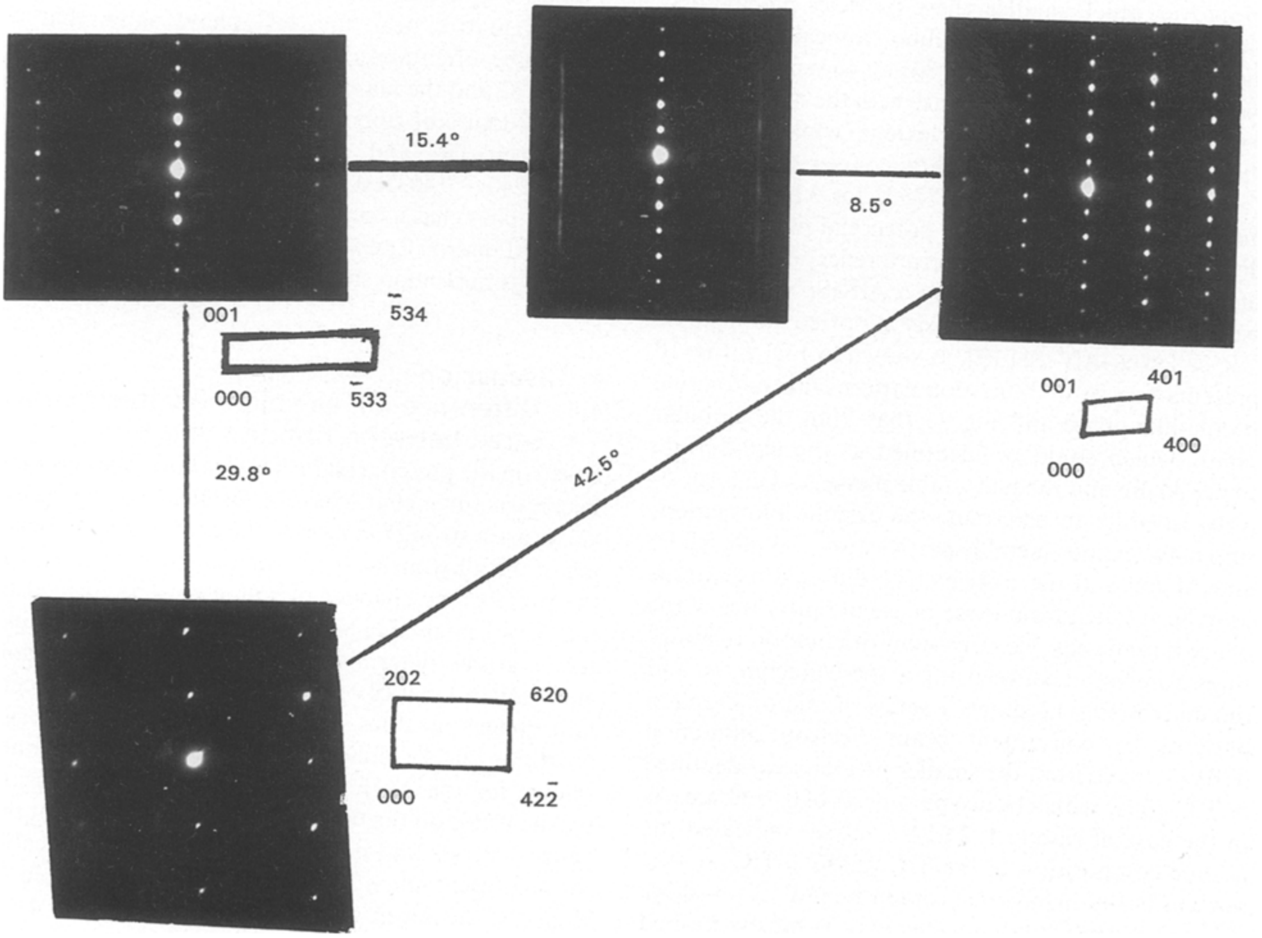

Figure 10 A series of diffraction patterns of Al_3Fe from Fig. 8(e).

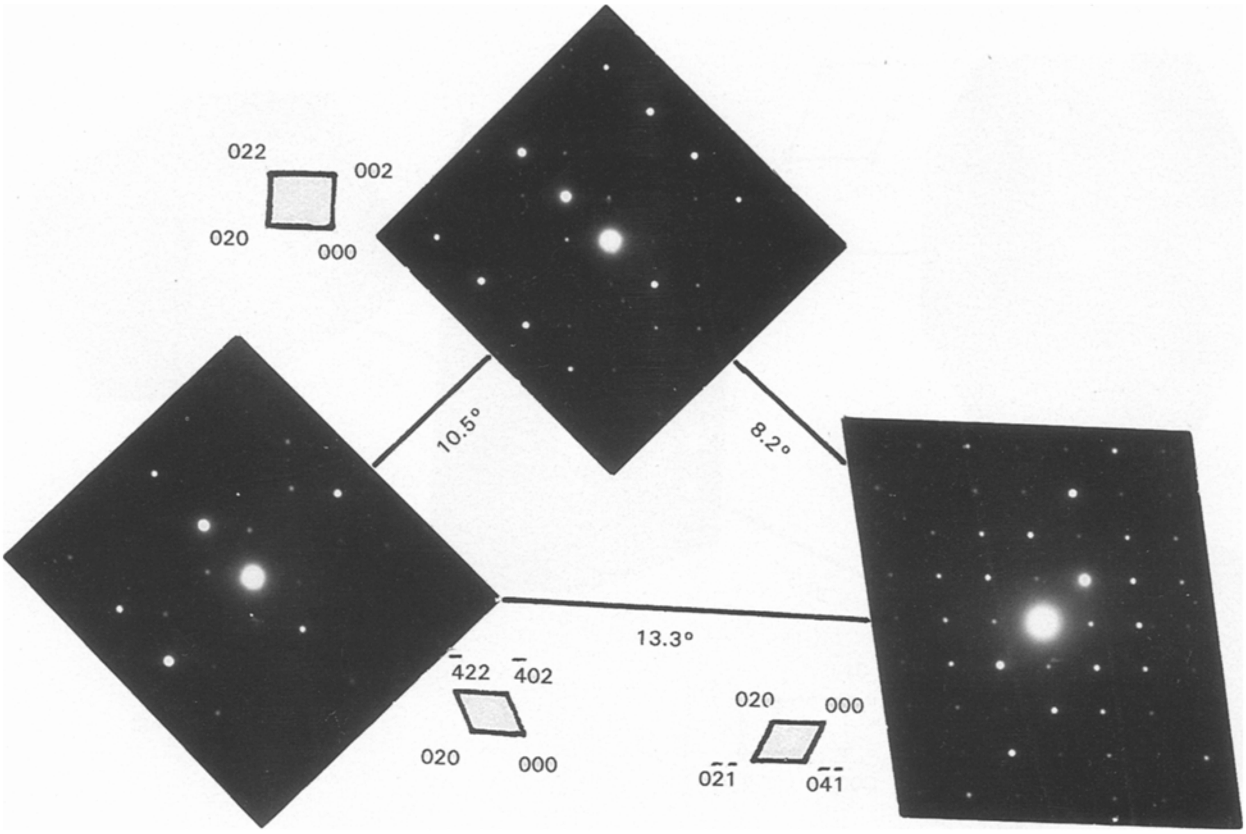

Figure 11 A series of diffraction patterns of Al_6Fe from Fig. 8(e).

needle-like particles and globular particles (Fig. 8(c)). Moreover, much smaller phase particles precipitated on the α-Al matrix. For the ribbon annealed at 673 K for 96 and 773 K for 5 h (Fig. 8(d, e)), the smaller phase basically remained a similar size with the number of its particles increased to some extent, while the other three larger phases were slightly coarser sequentially.

For the sample heated at 773 K for 5 h, a series of diffraction patterns from the polygonal phase may be described as weak superstructure reflections imposed on the basic b.c.c. structure of α-AlFeSi, which could be indexed using a previously reported monoclinic cell, called α_T-AlFeSi [10], as shown in Fig. 9. Fig. 10 presents a series of diffraction patterns taken from the needle-like phase and Fig. 11 that from the globular phase, which could be identified as the equilibrium phase Al_3Fe and the metastable phase Al_6Fe, respectively. In order to determine the orientation relationship between intermetallic particles (α_T-AlFeSi, Al_6Fe and Al_3Fe) and the α-Al matrix, diffraction patterns have been taken from these phase in both sides of the phase boundaries. No consistent orientation relationships were found between any of these precipitates and the matrix. Fig. 12 shows a series of microdiffraction patterns by convergent beam electron diffraction (CBED) taken from the smaller precipitates, identified as TiC phase with a lattice parameter of 0.4240 nm. As in the case of ribbon I, EELS analyses indicated the atomic composition of the TiC phase is $TiC_{0.79}$ (the same as in Fig. 3) (nominal composition $X_c/X_{Ti} = 0.74$), showing that the alloying elements Ti mostly formed into $TiC_{0.79}$ while the excess titanium was probably present in the particles of Al_3Fe or Al_6Fe, or retained in supersaturated solid solution in the α-Al matrix to some extent. Moreover, the microdiffraction analyses of α-Al matrix near the TiC phase show that a cube–cube orientation relationship was present between TiC and the matrix, as found in the as-solidified microstructure of ribbon I. In addition, a disregistry δ between TiC and α-Al could be calculated as $\delta = (0.4240 - 0.4031)/0.4240 = 0.049$. This showed that the TiC phase has a coherent or near coherent interface with α-Al matrix. Consequently, both TiC and α-Al can behave as nucleation sites during solidification.

4. Discussion

4.1. Difference of as-solidified microstructures between ribbon I and II

Based on the present results it is clear that the complex microstructures characteristic for RSP Al–Fe based alloys are a strong function of the degree of superheating of the alloy melts at the same quenching rates, i.e. the presence or changes of solute clusters formed in the liquid phase [11] as a function of superheating temperatures determine the competitive nucleation and growth kinetics of the various phases under certain quenching rates. Since the required free energy functions of the solid and liquid phases are only known for the Al–Fe system [9, 12], the discussion will be based on the binary Al–2 at % Fe alloy but the general trends and conclusions should be applicable to the present alloy. The detailed problems related to Ti and C, however, will be discussed in Section 4.2.

Fig. 13 shows a hypothetical metastable phase diagram for Al-rich aluminium iron alloys [9]. The

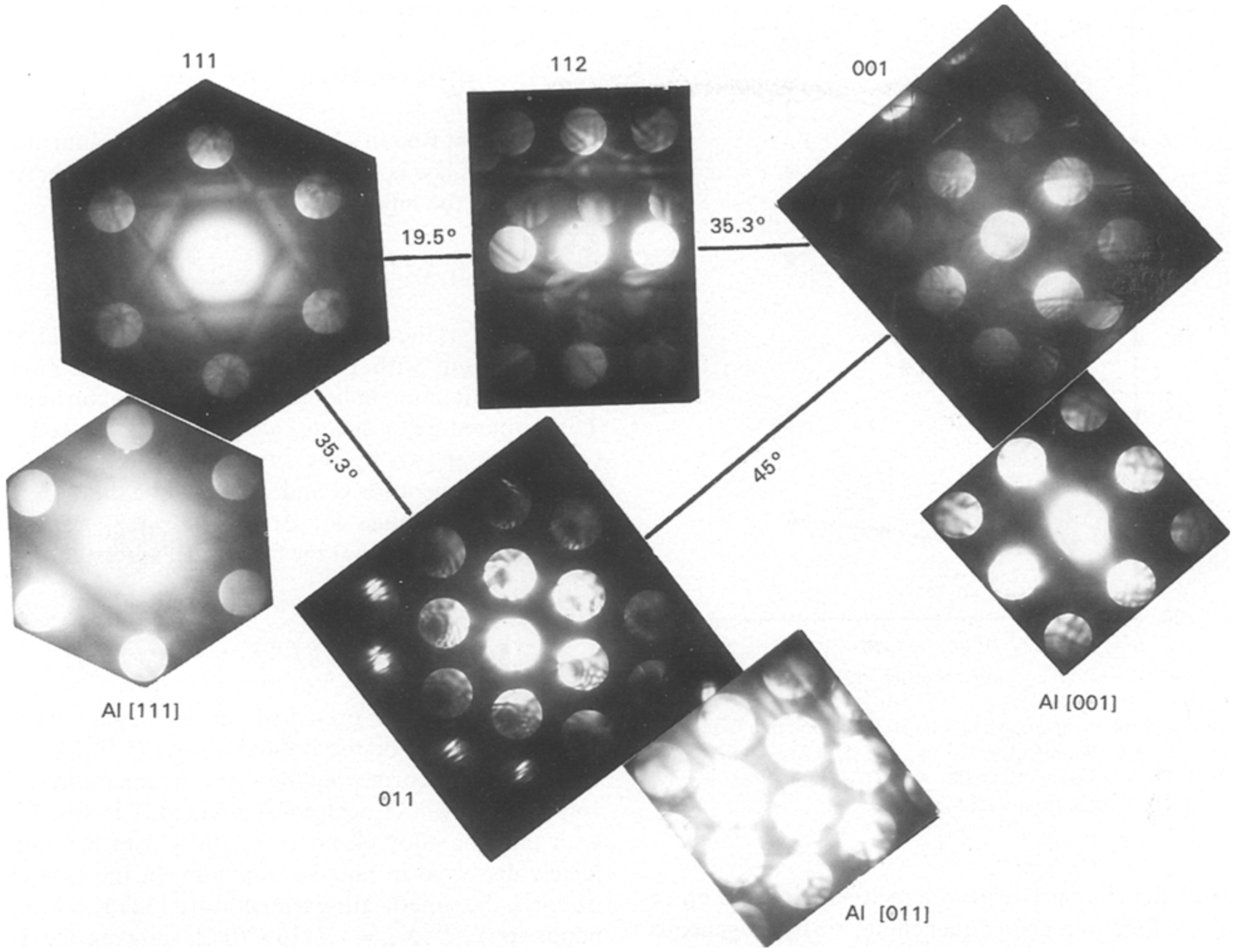

Figure 12 A series of microdiffraction patterns from TiC phase and α-Al matrix within the unit stereographic triangle.

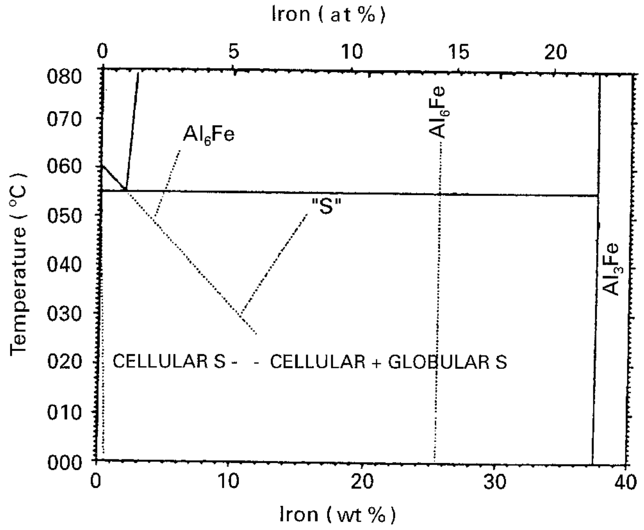

Figure 13 A hypothetical metastable phase diagram for Al-rich aluminium iron alloys showing the approximate location of the metastable "S" phase eutectic between α-Al solid solution and the Al_6Fe composition of the "S" phase [9].

liquidus and solidus have been extended by dotted lines. It is known that the formation of Al_3Fe can be suppressed even at low cooling rates and Al_6Fe forms with the approximate eutectic temperature and composition shown. At high solidification rates, the formation of Al_6Fe is suppressed and the "S" phase forms. In the case of ribbon I, the presence of the Al_3Fe, and especially TiC particles in the ribbon (Fig. 1) strongly suggests that the TiC and Al_3Fe were not completely dissolved during melting. Upon splat-quenching, TiC particles functioned as heterogeneous nucleation sites for α-Al phase. Continued undercooling of the remaining liquid results in the formation of dispersoids of Al_6Fe and new TiC (see following discussion) followed the microcellular growth of the Al–Al_6Fe degenerate eutectic (i.e. the formation of zone A). Since primary dispersoids are very small, they are readily pushed and trapped between the α-Al cells; however, part of TiC particles are engulfed inside cells. The above scenario accounts for the random orientations and high volume fractions of the Al_6Fe dispersions observed in the intercellular regions, as well as the exact orientations of TiC dispersions in the intracellular regions. During recalescence, associated with the rapid changes of structure (B zone), there are changes in the degree of segregation of Fe content. Despite the hypereutectic composition, the alloy solidified hypoeutectically (degenerated) in regions of quite high solidification rate developing an arrary of α-Al cells. On the other hand the low Fe content in the α-Al phase in coarser structures are reasonably related to lower quenching velocities and then, with mechanisms of solidification closer to equilibrium conditions (i.e. hypereutectic solidification) the remaining Al–Al_6Fe degenerated to eutectic solidification (C zone).

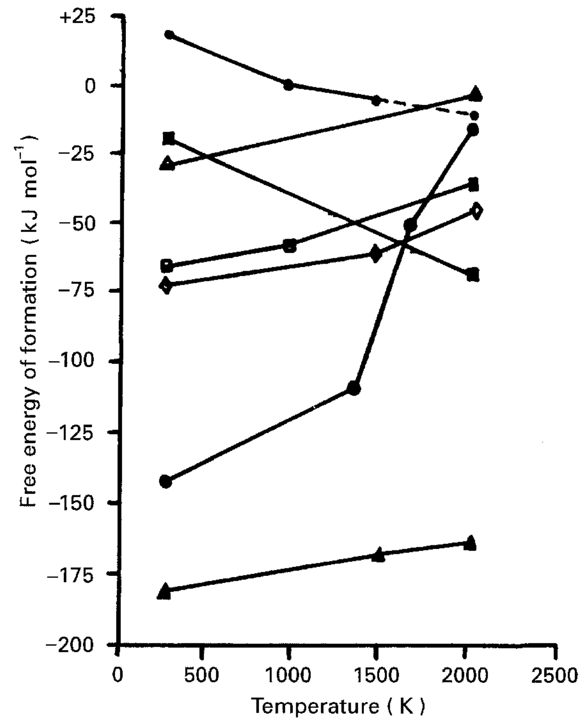

Figure 14 Free energy of formation (ΔG°) as a function of temperature for Fe_3C (●), SiC (◇), TiC (▲) and (1/3) Al_4C_3 (□) (datum from Ref. 13) as well as Al_6Fe (■), Al_3Fe (△) (datum from Ref. 12) and Al_3Ti (○) (data from Refs 14 and 15).

For the ribbon II with the melt superheated up to 1673 K for 5 min before quenching, the heterogeneous nucleation sites (e.g. Al_3Ti and TiC) have probably diminished in the largely purified melt. This can be confirmed in Figs 5 and 7. During quenching, a much higher undercooling could be reached (at least below T_0 temperature of α-Al) then that of ribbon I, so that the rapid solidification of the alloy would have happened in the temperature of the Al–"S" phase eutectic regions. Initially the α-Al firstly nucleated homogeneously and grew with extensive solute trapping of Fe, Ti and C elements; thereafter, the "S" phase formed between the α-Al grains. During recalescence, the Al_6Fe precipitated on the α-Al matrix grain. In annealing of ribbon II, the "S" (amorphous) phase transformed into α_T-AlFeSi phase with the composition near the "S" phase, while Al_3Fe was obtained following heat treatment with transformation from metastable phase (Al_6Fe) into equilibrium phase.

4.2. Formation of TiC phase

Fig. 14 compares the free energies of formation as a function of temperature for Al_6Fe, Al_3Fe and Al_3Ti as well as Al_4C_3, SiC and TiC on a per mole of carbon basis. On this basis, the formation of all these phases is possible, however, TiC has a substantially lower free energy of formation than other phases over the full range of temperature up to 2073 K. Therefore, both in liquid and in solid state of the alloy the formation of TiC should always be favourable.

In order to discuss the formation processing of TiC in the alloy, the following reaction will be analysed

$$\mathrm{Ti}(\beta) + \mathrm{C(s)} \rightarrow \mathrm{TiC} \qquad (1)$$

The change of free energy can now be written

$$\Delta G_{\mathrm{TiC}} = \Delta G^0_{\mathrm{TiC}} + RT \ln \frac{1}{a_{\mathrm{Ti}}\, a_{\mathrm{c}}} \qquad (2)$$

assuming that Roault's law is valid for aluminium and that Henry's law is valid for carbon and titanium. At equilibrium the following is obtained

$$\gamma^0_{\mathrm{C}} X^{\mathrm{L/TiC}}_{\mathrm{C}} \gamma^0_{\mathrm{Ti}} X^{\mathrm{L}}_{\mathrm{Ti}} = \exp \frac{\Delta G^0_{\mathrm{TiC}}}{RT} \qquad (3)$$

where $X^{\mathrm{L/TiC}}_{\mathrm{C}}$ is the mole fraction of carbon in liquid Al in equilibrium with graphite and $X^{\mathrm{L}}_{\mathrm{Ti}}$ is the mole fraction of titanium in liquid Al, R is the gas constant, T is temperature, *a* denotes activity of the respective component shown by the subscript, γ^0_{C}, γ^0_{Ti} are the activity coefficient for C and Ti at infinite dilution in liquid Al. The values for $\Delta G^0_{\mathrm{TiC}}$ and $\gamma^0_{\mathrm{C}}, \gamma^0_{\mathrm{Ti}}$ can be found in ref [15], so that the following expressions are obtained

$$X^{\mathrm{L/TiC}}_{\mathrm{C}} X^{\mathrm{L}}_{\mathrm{Ti}} = \exp\left(5.1298 - \frac{26\,865.472}{T}\right) \qquad (4)$$

This expression is presented in a diagrammatic form in Fig. 15. For the present alloy, $X^{\mathrm{L/TiC}}_{\mathrm{C}} X^{\mathrm{C}}_{\mathrm{Ti}} = 1.5925 \times 10^{-5}$, corresponding to a temperature of 1660 K. This is a critical point (marked A in Fig. 15) such that the alloy elements Ti and C can be completely dissolved in liquid aluminium. In the case of ribbon I, the superheating temperature 1523 K corresponds to $X^{\mathrm{L/TiC}}_{\mathrm{C}} X^{\mathrm{L}}_{\mathrm{Ti}} = 3.7116 \times 10^{-6}$, showing the Ti and C in the melt before quenching are mainly present

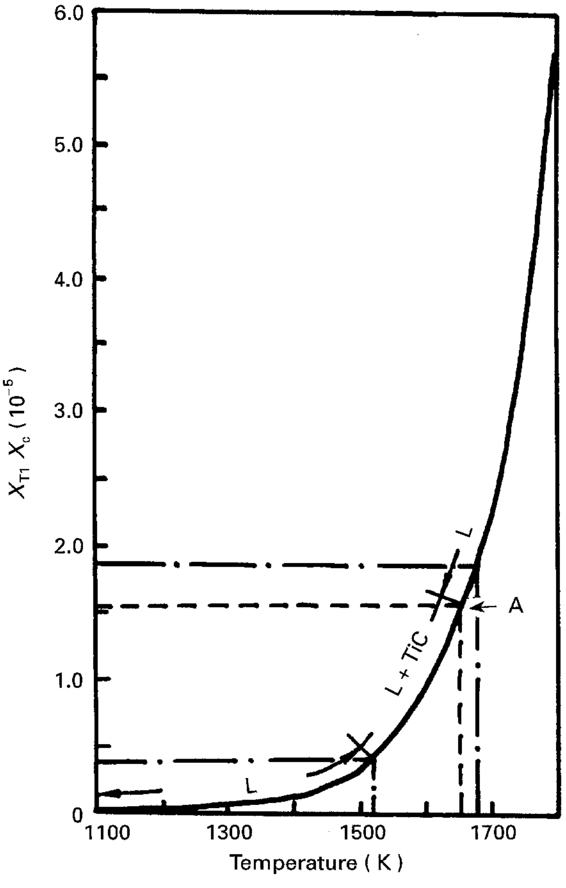

Figure 15 The stability diagram for TiC in the Al–Ti–C system.

in a form of TiC. During rapid solidification, the TiC particles were engulfed in the α-Al matrix serving as heterogeneous nucleation sites, as shown in Fig. 1. As for ribbon II, since the superheating temperature 1673 K is higher than the critical point temperature, 1660 K, the alloy elements Ti and C have completely dissolved in the liquid aluminium before quenching. At a very large undercooling the high growth velocity is sufficient to result in the trapping state of Ti and C in the α-Al, remaining at room temperature after quenching, as shown in Figs 5 and 7. During the annealing up to 673 K for 48 h the TiC precipitates on the α-Al matrix, as shown in Fig. 8. Consequently, the formation of TiC in the Al–Fe–Ti–C system is thermodynamically possible and practicable under certain dynamic conditions.

5. Conclusions

Based on the results shown above, the following conclusion have been drawn.

1. The rapid solidification of the Al–Fe–Ti–C alloy superheated to 1523 K before quenching (ribbon I) produced a duplex microstructure consisting of a microcellular region with segregate spacings of 40 to 60 nm (zone A), across a sharp transition (zone B), followed by a coarser cellular structure (zone C) which has a grain size about 10 times larger than that in the microcellular region. Most of the intercellular phases are the randomly orientated Al_6Fe, together with few of Al_3Fe phase. The dispersed TiC phase distributed on the α-Al matrix with an exact orientation relationship.

2. The rapid solidification of the Al–Fe–Ti–C alloy superheated to 1673 K for 5 min before quenching (ribbon II) has a uniform microstructure consisting of α-Al grains (with spacing of 0.15 to 0.3 μm). A high volume of globular Al_6Fe particles distributed uniformly in the grains, while larger size and elongated amorphous phase particles are located along the grain boundaries. Meanwhile, approximately 0.46 at % Ti and 0.35 at % C was dissolved in the α-Al matrix. During annealing, the amorphous phase transforms to α_T-AlFeSi phase, the Al_6Fe accumulated and Al_3Fe and TiC precipitated on the α-Al matrix.

3. The complex microstructures characteristic of RSP Al–Fe–Ti–C alloy are a strong function of the degree of superheating of the alloy melts. The rapid solidification of ribbon I is initially a heterogeneous nucleation process followed by the microcellular or cellular growth of the Al–Al_6Fe degenerate eutectic during recalescence. Ribbon II solidified as a homogeneous nucleation process under an undercooling large enough to result in the supersaturation of Ti and C in α-Al and coupled growth of amorphous phase. The Al_6Fe precipitated in the α-Al grains during recalescence.

4. TiC phase formed both in ribbon I and in heated ribbon II has an atomic composition of $TiC_{0.79}$ and a lattice parameter of 0.4240 nm. There is a cube–cube orientation relationship between precipitated $TiC_{0.79}$ and α-Al matrix with a disregistry of $\delta = 0.049$.

5. In the Al–Fe–Ti–C system, TiC has a substantially lower free energy of formation than other phases over the full range of temperatures up to 2073 K; i.e. both in liquid and in solid state of the alloy the formation of TiC should always be favourable thermodynamically. In the melt of ribbon I, The TiC particles have been formed before quenching and play the role of heterogeneous nucleation sites of α-Al phase during rapid solidification. For ribbon II, the alloy elements Ti and C have been completely supersaturated in the α-Al matrix during rapid solidification. The TiC precipitated in the α-Al matrix during annealing at the temperature range of 673 K for 96 h to 773 K for 5 h.

Acknowledgements

The authors wish to express their gratitude to G. X. Shi, G. J. Lei, Z. S. Yuong and S. K. Guan for kind help in experiments. This work was supported by NAMCC, contract No. 863-715026-02-02 and Henan Province Natural Science foundation, contract No. 934040100.

References

1. W. E. QUIST and R. E. LEWIS, in "Rapidly solidified powder aluminium alloy", edited by M. E. Fine and E. A. Starke (American Society for Testing and Materials, Philadelphia, 1986) p. 7.
2. W. M. GRIFFITH, R. E. SADERS, Jr and G. L. HILDEMAN, in "High-strength powder metallurgy aluminium alloys", edited by M. J. Koczak and G. J. Hildeman (The Metallurgical Society of AIME, Warrendale, PA, 1982) p. 209.
3. D. J. SKINNER, K. OKAZAKI and C. M. ADAMS, "Rapidly solidified powder aluminum alloys", edited by M. E. Fine and E. A. Starke (American Society for Testing and Materials, Philadelphia, 1986) p. 211.
4. M. H. JACOBS, A. G. DOGGETT and M. J. STOWELL, *J. Mater. Sci.* **10** (1974) 1631.
5. W. J. BOETTINGER, L. A. BENDERSKY and J. G. EARLY, *Metall. Trans.* **17A** (1986) 781.
6. M. G. CHU and D. A. GRANGER, *Ibid.* **21A** (1990) 205.
7. M. DeSANCIS, A. P. WOODFIELD and M. H. LORETO, *Inter. J. Rapid Solidification* **4** (1988) 53.
8. L. F. MONDOLFO, "Aluminium alloys: structure and properties" (Butterworths, New York 1976).
9. D. SHECHTMAN and L. J. SWARTZENDRUBER, "Alloy phase diagrams", edited by L. H. Bennett, T. B. Massalski and B. C. Giessen (Elsevier Science Publishing Co. Inc; New York, 1983) p. 265.
10. P. SKJERPE, *Metall. Trans.* **18A** (1987) 189.
11. P. J. BLACK and J. A. CUNDALL, *Acta Cryst.* **20** (1966) 417.
12. J. L. MURRAY, "Alloy phase diagrams", edited by L. H. Bennett, T. B. Massalski and B. C. Giessen (Elsevier Publishing Co., New York, 1983) p. 249.
13. "Smithells Metals Reference Book", edited by E. A. Brandes (Butterworth & Co. Ltd. London & Boston 1983).
14. J. L. MURRAY, *Metall. Trans.* **19A** (1988) 243.
15. A. JARFORS and H. FREDRIKSSON, *Microgravity Science and Technology, III* **4** (1991) 216.

Received 3 December 1993
and accepted 3 February 1995